Published online 3 October 2020

Nucleic Acids Research, 2020, Vol. 48, No. 19 ***e111***
doi: 10.1093/nar/gkaa782

A high-throughput alpha particle irradiation system for monitoring DNA damage repair, genome instability and screening in human cell and yeast model systems

Fintan K.T. Stanley [1,†], N. Daniel Berger[1,†], Dustin D. Pearson[1,†], John M. Danforth[1], Hali Morrison[2], James E. Johnston[1], Tyler S. Warnock[3], Darren R. Brenner[3], Jennifer A. Chan[4], Greg Pierce[2], Jennifer A. Cobb[1], Nicolas P. Ploquin[2] and Aaron A. Goodarzi [1,*]

[1]Robson DNA Science Centre, Departments of Biochemistry and Molecular Biology and Oncology, Charbonneau Cancer Institute, Cumming School of Medicine, University of Calgary, Calgary, Alberta, T2N 1N4, Canada, [2]Division of Medical Physics, Department of Oncology, Charbonneau Cancer Institute, Cumming School of Medicine, University of Calgary, Calgary, Alberta, T2N 1N4, Canada, [3]Robson DNA Science Centre, Departments of Cancer Epidemiology and Prevention Research and Community Health Sciences, Charbonneau Cancer Institute, Cumming School of Medicine, University of Calgary, Calgary, Alberta, T2N 1N4, Canada and [4]Department of Pathology and Laboratory Medicine, Charbonneau Cancer Institute, Cumming School of Medicine, University of Calgary, Calgary, Alberta, T2N 1N4, Canada

Received May 26, 2020; Revised August 27, 2020; Editorial Decision September 07, 2020; Accepted September 08, 2020

ABSTRACT

Ionizing radiation (IR) is environmentally prevalent and, depending on dose and linear energy transfer (LET), can elicit serious health effects by damaging DNA. Relative to low LET photon radiation (X-rays, gamma rays), higher LET particle radiation produces more disease causing, complex DNA damage that is substantially more challenging to resolve quickly or accurately. Despite the majority of human lifetime IR exposure involving long-term, repetitive, low doses of high LET alpha particles (e.g. radon gas inhalation), technological limitations to deliver alpha particles in the laboratory conveniently, repeatedly, over a prolonged period, in low doses and in an affordable, high-throughput manner have constrained DNA damage and repair research on this topic. To resolve this, we developed an inexpensive, high capacity, 96-well plate-compatible alpha particle irradiator capable of delivering adjustable, low mGy/s particle radiation doses in multiple model systems and on the benchtop of a standard laboratory. The system enables monitoring alpha particle effects on DNA damage repair and signalling, genome stability pathways, oxidative stress, cell cycle phase distribution, cell viability and clonogenic survival using numerous microscopy-based and physical techniques. Most importantly, this method is foundational for high-throughput genetic screening and small molecule testing in mammalian and yeast cells.

INTRODUCTION

Since the discovery of radioactivity more than a century ago, science has made extraordinary progress on understanding the effects of ionizing radiation (IR) on the health of living organisms, with particular emphasis on the impact of IR on DNA (1,2). The use of human cell lines and genetically tractable models such as yeast has revealed an array of pathways responsible for preserving genomic stability following IR exposure (3). This research has, in turn, provided an understanding of human disease susceptibility, genetic syndromes and has given rise to high specificity anti-cancer agents (4,5). Overwhelmingly, IR research has focused on understanding the effects of 'sparsely' ionizing, low linear energy transfer (LET) photon radiation such as X-rays or gamma rays, as these penetrate aqueous media, glass and/or plastic with ease, and can be generated cheaply and conveniently. By comparison, more 'densely' ionizing, higher LET particle radiation including protons, neutrons, alpha particles (helium ions) and high (H) atomic number (Z) and energy (E) (HZE) ions have been understudied, as they are more challenging to produce and deliver in a controlled manner. Such particles do not easily penetrate media, flasks, dishes or slides and/or can require expensive technology to generate (2,6–10). Indeed, restricted and time-limited access to costly accelerators confines that type work to a small minority of re-

*To whom correspondence should be addressed. Tel: +1 403 220 4896; Email: A.Goodarzi@ucalgary.ca
†The authors wish it to be known that, in their opinion, the first three authors should be regarded as Joint First Authors.

searchers and makes certain experiments—such as repetitive particle exposure work—uneconomical and/or impractical. While there are certainly economical particle IR protocols available (9,11–17), most of these are not well suited for very high-throughput experimental modalities, still require cell culture on ultra-thin plastic film, and/or have not been adopted widely by radiation researchers for very different experimental endpoints and model organisms using the same controlled setup.

The impact of this logistical bottleneck on particle radiation research has been substantial. Less than 2% of human cell-based IR studies and <1% of yeast-based IR studies in the PubMed literature include the search terms 'high LET' or 'particle'. Consequently, our knowledge of the biology underpinning IR-vulnerable populations and IR-sensitive tissues or cell types is mainly derived from high dose (>100 mGy), acute exposure photon radiation research. This is problematic, as the majority of human lifetime IR exposure is via repetitive or chronic, low levels of particle radiation partly from cosmic ray HZE particles, but mostly from alpha particles arising from decaying gaseous terrestrial ^{222}Rn and related radioisotopes (2,18,19). Further, risk models and health protection policies are often built on data derived or extrapolated from high dose photon radiation studies, whose observations have an ambiguous or reduced relevance to the realities of low dose and/or particle IR effects (20,21). Controversial theories such as 'hormesis' (i.e. above background but low IR doses are 'beneficial') continue to be debated but are largely based on photon radiation findings that do not apply to particle radiation. Indeed, what we do know about high LET radiobiology indicates a substantially more complex spectrum of DNA damage induction, slower DNA repair kinetics, reduced DNA repair accuracy, differently utilized DNA repair pathways and, for a given dose, a considerably greater propensity to trigger disease (7,9,22–29).

The *International Commission on Radiological Protection* Report 103 describes the biological weighting of alpha particles as 20 versus 1 for photons (30). While this is important, we need better, molecular-level detail of high LET IR biology to establish the specific genetic, cellular and tissue context of risk, and to discover interventions that modify exposure consequences to mitigate dangers to health. Prevalent ^{222}Rn exposure, the prospect of manned Mars exploration, and possible particle-associated pathologies such as myalgic encephalomyelitis highlight the need to know how particle exposure impacts health in exquisite detail (31–41). This will require high-throughput, affordable and widely accessible technology to achieve. Here, we describe a new and versatile method to deliver alpha particles at the benchtop of a standard laboratory. This represents an important advance over previous methodologies (9,11–17) as it (i) avoids the need for particle accelerators or culturing cells on fragile plastic films; (ii) increases convenience, throughput and capacity; (iii) is derived from commercially available, inexpensive materials; (iv) is adjustable but accurate and precise in dose; and (v) the same system is applicable to multiple experimental endpoints, yeast and mammalian cell model systems and prolonged repetitive or chronic irradiation experiments.

MATERIALS AND METHODS

Particle irradiator scaffold design and ^{241}Am source recovery

All 3D designs for novel particle irradiator scaffold were created in SketchUp Free (2017 version, Trimble) and AutoDesk Fusion 360 (version 2.0.6037), converted to the .stl file format and prepared for 3D printing in Ultimaker Cura 3.5 (Ultimaker). Printing was carried out on the Ultimaker2 platform using PLA plastic. All template files are available in Supplementary Data for download. ^{241}Am sources were recovered from Kidde Pro Series Direct Wired smoke detectors (Home Depot, Canada) according to the detailed protocol outlined in Detailed Protocol 1 (see supplemental information). Permission and approval to disassemble ^{241}Am smoke detectors was obtained via the University of Calgary Radiation Safety Office and the Canadian Nuclear Safety Commission. Extracted sources were stored in lead containers when not in use. Custom electrodeposited ^{241}Am sources used for smoke detector source dose calibration were received from the National Research Council of Canada (NRC).

^{241}Am alpha particle source dosimetry and calibration

EBT3 GafChromic film (Ashland Specialty Ingredients, Wayne, NJ) was used to quantify the dose rate of 72 independent ^{241}Am sources. EBT3 GafChromic film has a dynamic range from 0.1 Gy to upwards of 10 Gy, has submillimetre spatial resolution, minimal energy dependence with photons, develops in real time with radiation dose (i.e. does not require any chemical processing or fixation), and has near tissue-equivalence. For these reasons, it is frequently employed to perform absolute dosimetry in the context of radiation therapy (42–45). EBT3 film is composed of a 28 μm radiation sensitive layer between two 125 μm matte polyester layers. The top polyester layer was removed for the purposes of this study, as the path length of the alpha particles emitted by ^{241}Am (∼35 μm in polyester and ∼43 μm in water, based on (46), is too short to penetrate beyond the surface layer of the film. Uniformity of the film was not found to degrade after splitting it. The split film was calibrated with a high energy linear accelerator (Varian TrueBeam linac [Varian, Palo Alto, CA]) using a 6 MV photon beam from 0 to 6 Gy. All films were scanned with an Epson Expression 12000XL flatbed scanner (Seiko Epson Corp., Nagano, Japan). The film calibration was performed as in (47). The scanned optical densities were converted to dose using a Triple-channel heterogeneity correction method, utilizing all three colour channels (red, green and blue) from the scanned image to correct for film thickness heterogeneities (48). EBT film however displays an under-response (less darkening) with high-LET particles due to an LET quenching effect resulting in lower polymerization yield compared to low-LET radiation (44,49–52). This has not been previously quantified for EBT3 films at the low energies (and high-LET values) utilized here. To quantify this effect, a calibrated source was used to irradiate the split film and the dose was calculated using the MCNP6 (v6.2) Monte Carlo (MC) package

(53) as well as using the 6 MV calibration curve. The calibrated source consisted of electrodeposited ^{241}Am on an aluminum planchet with known active diameter, activity, emission spectrum and emission rate. A 3D printed holder was created to place the source above the film at a known and reproducible distance. The difference in doses was used to correct for this effect. MC simulations were also used to determine the dose received by the cell layers in relation to the dose received by the 28 μm thick layer of film using the measured geometry and energy spectrum for the smoke detector source. The human fibroblast cells were modelled as a 10 μm thick layer below a 20 μm thick layer of water, and the yeast cells were modelled as a 3.5 μm thick layer at the surface. The energy and LET of the alpha particles will change as they pass through air and the film or cells. This was also quantified from the Monte Carlo simulations and the weighted mean LET was found to range from 120.9 to 199.8 keV/μm for all possible distances, with a practical LET range of just ±9 keV/μm (159–168 keV/μm) for the actual experimental set-ups used in this study. For the measurements with the smoke detector sources, to achieve the appropriate dose level, the split EBT3 film was exposed to the ^{241}Am sources for 8 min. Three exposures were performed for each source that were used to calculate an average dose rate for each source in mGy/s. The reproducibility of the repeated measurements was 1.5% on average, with a maximum deviation of 6.0% for the total of 72 sources measured. Source to source dose rate variations were found to be ±9.4% (i.e. the difference in activity of sources). The uncertainty in dose is estimated to be 10.3% ($k = 1$), which includes the source to source variability, the statistical uncertainty in the MC simulations, the film measurement uncertainty (of the calibrated source and the smoke detector sources) and the uncertainty in the calibrated source activity.

Human cell lines

Human cell cultures were maintained at 37°C, 5% CO_2 in a humidified atmosphere. 48BR primary human fibroblasts were obtained from the Jeggo laboratory (University of Sussex, UK) and are described in detail in (23,54,55). 48BR were cultured in DMEM (Gibco #11995–065) + 15% (v/v) fetal bovine serum (FBS, Gibco #12483–020) and 1% (w/v) penicillin–streptomycin (Gibco 15070–063) and 1% (v/v) Glutamax (Gibco #35050–061). A549 (ATCC #CCL-185) and Hela cells (ATCC #CCL-2) (and their gene-edited versions (56)) were maintained in DMEM + 5% (v/v) FBS and 5% (v/v) HyClone Serum (GE #SH30109.03), with 1% penicillin–streptomycin and 1% Glutamax. RPE-1 cells (ATCC #CRL-4000) were maintained in DMEM:F12 (Gibco #11330–032) + 10% (v/v) FBS and 0.01 mg/ml Hygromycin (Sigma, #10687010). WI-38 cells (ATCC #CCL-75) were maintained in EMEM (ATCC #30–2003) + 10% (v/v) FBS with 1% (w/v) penicillin–streptomycin and 1% Glutamax. All cell lines are tested regularly for mycoplasma and confirmed to be negative. Cell line identity was confirmed by gene sequencing. Cells were passaged regularly and seeded in 96 well optical glass plates (Cellvis #P96–1.5P).

Yeast strains

All *Saccharomyces cerevisiae* strains are derived from JKM 179 (57). Wild-type MAT**a** *ade-1 leu2–3, 112 lys5 trp1::hisG ura3–52*, *hml::ADE1*, *hmr::ADE2*, *ade3::GALHO*, and either *rad50Δ::URA3 or nej1Δ::KanMX6*. Yeast culturing and plating was done using YPAD broth or agar. YPAD was prepared in ddH_2O with 1% (w/v) Bacto-yeast extract (BD Biosciences, #212750), 2% (w/v) dextrose (Sigma, #D1912), 2% (w/v) Bacto peptone (BD Biosciences, #211677), and supplemented with 25 μg/ml adenine (Sigma, #A8626), with 2% (w/v) Difco agar (BD Biosciences, #214530) for plates. Yeast cultures were grown overnight in 1 ml of YPAD media in a rotary shaker at 30°C and 220 rpm.

Small molecule compounds

ATM inhibitor (ATMi = KU55933, Calbiochem #118500–2MG), DNA-PKcs inhibitor (DPKi = NU7441, Selleck Chemicals #S2638) and Poly(ADP-Ribose) Polymerase inhibitor (PARPi = AZD2281, Selleck Chemicals #S1060) were made into 50 mM stock solutions in molecular biology grade 99.9% DMSO (Sigma, #D8418), stored at −80°C, diluted to 1000× working concentration and added to cell media (ATMi at 10 μM; DPKi at 5 μM, PARPi at 2.5 μM) 1 h before irradiation. From Tocris we obtained Poly(ADP) Ribose Glycohydrolase (PARG) inhibitor (PARGi) PDD00017273. The radioprotectant small molecule, myricetin (Sigma #M6760) and epicatechin (Sigma #E4018), were prepared as 100 mM stock solutions in 99.9% molecular biology grade DMSO (Sigma, #D8418) and used at 20 and 30 μM, respectively. Additionally, the Bowmann-Birk Inhibitor peptide (GPKKKRKV KSCICALSYPAQCFYPYDVPDYA, >98% purity, synthesized by BioBasic, Canada) was prepared as 100 mM stocks in PBS and used at 10 μM. Staurosporine was from Sigma (#S5921), dissolved in DMSO to a stock concentration of 10 mM and used at 1 μM.

Photon and particle irradiation protocol

Unless otherwise indicated, cells were irradiated at room temperature. For particle irradiation, cells were plated in 5 μl droplets in the center of each well of the 96-well optical glass plate (Cellvis #P96–1.5P) using the custom centre-plating pipettor guide, allowed to adhere for 8 h, and then carefully topped up with 195 μl media. For particle irradiation in the context of imaging experiments, media were removed, and alpha sources were inserted into respective wells for the designated time (no longer than a 3-min fraction), after which the apparatus was removed, and the media replaced. Fractionation regimens were performed to minimize the time cells were exposed to increased aeration. For photon irradiation using gamma rays, cells were irradiated using a GammaCell 1000 Elite source (MDS Nordion), which contains a ^{137}Cs source that emits approximately 2.9 Gy/min. As 96-well plates cannot fit within a typical GammaCell irradiator, photon irradiation experiments using 96-well plates used X-ray irradiation via a Varian TrueBeam Linear Accelerator (LINAC). A CT scan of the 96-well plate

with the same amount of medium as planned for during irradiation was acquired. A treatment plan was created to determine the homogeneous dose (±5%) to be delivered to the medium in the 96-well plate. The single created treatment plan was used for guiding the dose to be delivered for each cell irradiation. A custom fit heat moulded plastic jig was fabricated to provide full lateral photon scatter conditions to the 96-well plate. About 5 cm of Solid Water High Equivalency (Standard Imaging) slabs were placed under the 96-well plate to provide full backscatter conditions and 2 cm above it to provide full charged particle equilibrium conditions. Using the in-room lasers and the crosshair of the LINAC, the 96-well plate was aligned with the treatment couch and gantry in a reproducible, consistent manner to deliver the calculated dose by the planning system. As per the treatment plan, a field size of $X = 15$ cm and $Y = 10$ cm was used, with a Source to Surface Distance (SSD) of 96 cm. About 2.4 Gy (or a calculated 235 monitor units) of 6 MV X-rays were delivered with a dose rate of 300 MU/min on the Varian TrueBeam LINAC. The 96-well plates and cells contained in them were at room temperature for the duration of the irradiation, approximately 15 min.

Immunofluorescence

For general imaging experiments, 5000 cells were plated in their final culture volume (200 μl/well) 48 h prior to first irradiation. Cells were fixed with 3% (w/v) PFA, 2% (w/v) sucrose in 1× PBS at the indicated time points at room temperature for 10 min. Working gently with a multichannel pipette, cells were washed three times with 1× PBS + 0.05% (v/v) Tween 20 (PBST) and permeabilized in 1× PBS + 0.5% (v/v) Triton X-100 for 10 minutes at room temperature. Cells were washed three times with PBST, before being blocked in 3% (w/v) normal goat serum (NGS) in PBST for 10 min at room temperature then washed three times in PBST. Cells were then incubated with primary antibodies in 1% NGS in PBST for 1 h at room temperature and washed three times in PBST after. Cells were then incubated with secondary antibodies in 1% NGS/PBST for 30 min at room temperature, washed once with PBST, and counterstained with DAPI (1:10,000) 10 min and finally washed three times with PBST. Wells were then filled with PBS with 0.05% (w/v) sodium azide. Confocal images were acquired on a LSM880 Carl Zeiss confocal microscope, with a Plan Apochromat 20 × /0.8 NA, EC Plan Neofluar 40 × /0.75 NA and Plan Apochromat 63 × /1.4 NA (oil immersion) objective, using AxioCam MRm Rev.3 camera, and processed for false colorization, overlay/colocalization, orientation and scale with Zeiss Zen Lite. Widefield images were acquired on a Zeiss Axio Observer Z1 platform microscope with an EC Plan-Neofluar 40x/0.75 NA objective and an AxioCam MRm Rev.3 camera. Representative images were deconvolved and maximum orthogonally projected using Zeiss Zen desktop software (version 3.1). 3D analysis was performed with TANGO (Fiji plugin). Glycerol or Fluoromount G (EMS #17984–25) was used for longer term storage of samples. The following primary and secondary antibodies were used in the following concentrations: 53BP1 (Rabbit, Abcam ab21083, 1:400); γH2AX (Mouse, Abcam ab26350, 1:800); PAR (Rabbit, Trevigen 4336-BPC-100, 1:200); Alexa Fluor 488 (Goat, Invitrogen A-11001, 1:800); Alexa Fluor 594 (Goat, Invitrogen A-11012, 1:800).

Automated γH2AX signal quantification

Analysis and graphing were carried out using Excel (version 16.0.6769.2017, Microsoft), GraphPad Prism (version 8.1.2, GraphPad), RStudio (version 1.1.456, RStudio), Zen Blue (version 2.6, Zeiss), TANGO (version 0.98, TANGO) and R (version 3.6.0, R Core Team). Images were all acquired on Zeiss systems and saved as .czi files. These files were imported into ImageJ/FIJI (version 1.52p) using the Bioformats plugin. A detailed protocol on how to set up TANGO for this methodology is described in **Detailed Protocol 2** (see supplemental information). Within TANGO, the imported images were pre-filtered with Fast-filters 3D (median, with a RadXY size of 3 and RadZ size of 2) for each *z*-stack, followed by nuclei segmentation using Renyi Entropy Auto thresholding for Simple Segmenter. Post-filters were applied to fill any holes arising from segmenting using 'Fill holes 2D', 'Binary Close' with a *XY*-radius of 10 (using the image scale for the *Z*-radius) and a second 'Fill holes 2D' of 'Morphological Filters 3D' followed by a 'size and edge filter' to remove nuclei touching the image boundary. Incorrectly segmented nuclei were manually removed. To analyze the γH2AX signal, an initial sliding paraboloid 2D background subtraction (with a pixel radius of 25) and Fast Filters 3D (median, with a RadXY size of 1 and RadZ size of 1) was applied to each *Z*-stack. Spot detection used the Renyi Entropy method to automatically detect and segment γH2AX signal within the nuclei. The Hessian Scale was set to 1 and all other limits were set to Autothreshold using Renyi Entropy. Post filters were applied to remove any signal found outside the nuclear segmentation or totaling <2-pixel area (template processing chain files available upon request). Once the nuclear and γH2AX segmentation was run, images were tagged by condition and measurements (Measure Geometrical Simple and Signal Quantifications) were exported based on mapping these voxel volumes to the original data. The details of the analysis are outlined in the supplied R markdown file, with each line of code annotated. The workflow in Figure 2D summarizes this method.

Alkaline comet assay

Alkaline comet assays were performed as per (58) and (59), with some modifications. For alkaline comet assays with particle radiation, 1000 cells were centre-plated in a 5 μl droplet in the centre of a 96-well plate well and allowed to adhere for 8 h before being topped up with 195 μl cell media. For fractionated IR, 2-min particle or photon fractions were separated with 5 min recovery periods in warm (37°C) media or cold (4°C) 1× PBS. For particle IR, cells were irradiated with eight fractions of alpha particles or sham control, with 8 wells per condition, and (following the final fraction) immediately trypsinized and collected. For photon alkaline comet assays, cells were trypsinized and resuspended in either cold 1× PBS or warm media at a dilution of 1000 cells/ml. Cells were then irradiated with eight fractions of gamma IR with only the absolute dose of photon IR differing from the particle conditions. Cells in both particle

and photon conditions were then washed in pre-chilled 1× PBS, spun down at 1500 rpm for 3 min and resuspended in 150 μl of cold 1× PBS. Cells were mixed with an equal volume of 1.2% (w/v) low melting point agarose (Invitrogen, #16520–050), and quickly layered onto a pre-chilled frosted glass slide with a 0.8% (w/v) ultrapure agarose (Techologist Choice #7109) base layer. Coverslips were used to maintain the agarose shape, and slides were chilled at 4°C in the dark until set. Coverslips were removed, and slides were immersed in pre-chilled lysis buffer (2.5 M NaCl, 10 mM Tris-HCl, 100 mM EDTA, 1% (v/v) Triton X-100, 10% (v/v) DMSO, pH 10) for 1 h in the dark, then washed three times with pre-chilled electrophoresis buffer (50 mM NaOH, 1 mM EDTA, 10% (v/v) DMSO). Slides were placed in electrophoresis chamber with buffer, and allowed to equilibrate for 45 min before being electrophoresed at 25 V for 25 min (0.6 V/cm), and neutralized with Tris-HCl pH 7.4 for 1 h at 4°C. DNA was stained with SYBR Green (1:10,000 from Sigma #S9430) and 0.5% antifade (0.5% (w/v) p-phenylenediamine in 20 mM Tris, pH 8.8, 90% (v/v) glycerol) for 10 min at room temperature. Slides were imaged and Comet Assay IV (Perceptive Instruments, UK) software was used to quantify tail moment for at least 100 cells per experiment.

H_2DCFDA oxidative stress assay

H_2DCFDA (ThermoFisher, D399–100 mg) was prepared as a stock at 20 mM in DMSO and diluted to final concentration of 20 μM in media. 20 μM H_2DCFDA was loaded into centre-plated cells for 1 h at 37°C, 5% CO_2. For particle IR, cells were exposed to either one or eight fractions of particle IR, and sham controls experienced media removal, but no IR. For photon IR, cells were exposed to one or eight fractions of X-ray IR on a Varian TrueBeam LINAC in an equivalent experimental setup (administered to mimic particle IR conditions). A 5-min exposure to 1 mM H_2O_2 in 1× PBS was added as a positive control. Following the final fraction, residual media were gently washed from wells once with cold 1× PBS, and media were replaced with cold 1× PBS to avoid media autofluorescence. Ten minutes following the final fraction, the resulting DCF fluorescence was read on a Molecular Devices SpectraMax iD3 microplate reader with filters set for an excitation of 485 nm and emission of 535 nm. For each experiment, the fluorescence values of 6 wells were averaged together.

Alamar blue cell viability assay

For viability assays, 1000 cells were centre-plated in a 5 μl droplet in the centre of a 96-well plate and allowed to adhere for 8 h before being topped up with 195 μl cell media. Cells were then exposed to particle IR. Twenty-four hours post irradiation, Alamar Blue (Thermofisher, #DAL1100) was added to a final concentration of 10% (v/v), and cells were allowed to metabolize the dye for 8 h. Fluorescence was then read on a Molecular Devices SpectraMax iD3 plate reader, with excitation at 560 nm and emission at 600 nm. A fluorescence correction was performed on empty media to determine percent dye reduced, and data were normalized to untreated, unirradiated cells.

Clonogenic survival assay

For these assays, please note that the particle IR source was raised to a height of 2.25 mm to provide better IR coverage of centre-plated cells. For the survival assays, 1000 RPE-1 hTERT cells were centered-plated in a 5 μl droplet in the centre of a 96-well plate and allowed to adhere for 8 h before being topped up with 195 μl cell media. If desired, cells may be incubated small molecules (we used 10 μM ATMi for 1 h) for a desired time period prior to particle irradiation, followed by 2 min fractions separated with 5 min recovery periods in media. After the final fraction, cells recovered for 1 h then were trypsinized and transferred (with three washes to ensure maximum cell transfer) into 6 cm dishes with 6 ml of cell media. For IR doses >0.2 Gy, multiple wells were pooled to plate up to 10 000 cells to obtain countable colony numbers (users will need to calculate this for their specific cell line and/or cell treatment context). Cells were allowed to grow for 7–8 days then washed twice with PBS, fixed in a 1:7 solution of acetic acid:methanol for 10 min, then stained in a filtered 0.5% Crystal Violet solution for 2 h. Colony enumeration was carried out by hand and for each condition, all fractions were carried out in duplicate and repeated over three independent experiments. The plating efficiency was calculated based on the number of colonies formed in the untreated cells with all conditions normalized to the untreated.

Yeast survival assays

For both drop assay and survival assays, yeast concentrations were determined using a hemocytometer and diluted to the desired concentrations in ddH_2O. Aliquots of 1 μl of suspension were dropped on YPAD plates prior to treatment. Yeast were either plated on 86 × 128 mm Nunc OmniTray single-well plates (ThermoFisher), or 60-mm culture dishes for alpha or gamma irradiation, respectively. Yeast for drop assays were plated in a 1:10 dilution series from an initial concentration of 8×10^7 cells/ml. After plating, droplets were allowed to dry for 15 min before being handled to avoid smearing. Yeast were irradiated with doses of 0.457 ± 0.019, 0.915 ± 0.038, 1.830 ± 0.077, 2.745 ± 0.115 or 5.490 ± 0.230 kGy at room temperature, with a row of non-irradiated controls. After irradiation, yeast cells recovered at 30°C and 0.5% CO_2 for 10 h before imaging. Alpha particle survival assays were performed by plating 500 cells/plate and irradiating with the same doses as the drop assay and were cultured in the same conditions for 24 h post-irradiation. During optimization, it was found that the 2.745 and 5.490 kGy doses resulted in either no colonies forming or one at most, so 5000 and 50 000 cells were irradiated for these time points, respectively, to achieve better quantification. Results from both assays were imaged using an ImageQuant LAS 4000 (GE Healthcare) and colonies were manually counted.

Statistical analysis

Statistical analysis was performed using GraphPad Prism 8 software. Dots in dot plots represent values of single cells, and the mean ± SEM of at least three independent experimental repeats is shown. Data were evaluated by one-way

or two-way analysis of variance (ANOVA) followed by the Tukey's test, or alternatively a two-tailed Student's *t*-test. A value of $P < 0.05$ was considered to be significant. For all tests, *P*-values as follows: n.s. = non-significant (>0.05); * = statistically significant (<0.05); ** = statistically significant (<0.01); *** = statistically significant (<0.001); **** = statistically significant (<0.0001). Experiments were repeated a sufficient independent number of times to ensure reproducibility of results. See specific figure legends for details.

RESULTS

Design and construction

Previously described alpha particle irradiators for the standard laboratory predominantly involve growing human cells on ultra-thin polypropylene or polyester (Mylar) plastic film with inverted irradiation, often via sources such as ^{241}Am or accelerators (9,10). Whilst practical for modest cell numbers (10^2–10^6), throughput is constrained with this method. Furthermore, thin plastic film can present greater logistical challenges, and may preclude work with primary and/or differentiated cells. To resolve these problems, we set out six conditions for a new design: (i) compatibility with high throughput infrastructure (e.g. a 96-well plate), (ii) affordable and simple to construct, (iii) resilience and resistance to human error, (iv) accurate and precise dose delivery with an adjustable low dose rate, (v) capacity to irradiate $\geq 10^6$ cells per experiment and (vi) adaptability to model organisms. We selected a low-cost alpha IR source compatible with glass-bottomed 96 well plates. ^{241}Am is a synthetic radioisotope with a 432-year half-life (permitting a functionally steady dose rate over a human lifetime) that emits 5.486 MeV alpha particles with a minor 59.540 keV gamma emission (60). This compares closely to the 5.489 MeV alpha particle energy emitted during ^{222}Rn decay, making it ideal to model radon exposure. Sources may be custom-ordered from suppliers (e.g. Eckert & Ziegler), but are also manufactured as components of smoke detectors. Legal permission to disassemble retail smoke detectors for research may be (and was) obtained from atomic energy regulators and is a straightforward, safe procedure. Alternatively, ^{241}Am sources for smoke detector production may be obtained from suppliers directly. Such ^{241}Am alloys are housed within a metallic casing whose dimensions fit within a standard well of a 96-well plate (Figure 1A). Using computer-aided design and 3D printing, we built a custom 96-well plate-compatible bracketing-and-scaffold system to irradiate adherent cells. The design is based on a peg bracket each with one ^{241}Am source and is scalable so that all 96 wells can be irradiated simultaneously (Figure 1A and B).

Alpha particle dosimetry validation

About 5.486 MeV alpha particles have a path length of 41.5 mm in dry air, but only 43 μm in water—meaning that particles will traverse the 11.7 mm depth of a 96-well plate to deposit energy beneath (46,60). Precise doses may be calculated by knowing distances between ^{241}Am and the target surface, and accounting for surface features (in our case, either split EBT3 film, a yeast colony on solid media or human cell monolayers in residual media; see 'Materials and Methods' section for details) (Figure 1C). We engineered removable pegs of an exact length to obtain a source-to-target distance of 0–1.75 mm, with ≤15 μm variation, and measured the dosimetry of our ^{241}Am sources using alpha-sensitized (split) EBT3 film, together with a calibrated ('known quantity') ^{241}Am disk provided by the National Research Council (Canada) (Figure 1D and E). Splitting the EBT3 film was required to permit alpha particles to register a signal, and we confirmed that the uniformity of the film was not degraded after the splitting process. Photon emissions were not detectable, even with multiple day exposures. For human cell monolayers, the device had a 5.75 mGy/s irradiation rate at 0.38 mm from film (a practical irradiation distance for human cells) (Figure 1F, left). Regression indicates a dose rate of 0.005 mGy/s is achievable at the maximum distance of 10 mm, a dynamic range that is readily compatible with high-to-low dose rate particle experimentation (Figure 1F, right). For the distances used in this study (0.1–2.25 mm), a relatively narrow LET range of ± 9 keV/μm (i.e. 159–168 keV/μm) was obtained, indicating that differing LET is not a major variable (Figure 1G). For most human cell work in this study, our 'default' dose was a 2-min exposure at the 0.38 mm distance, equating to 0.692 ± 0.071 Gy. For simplicity, we will henceforth refer to this as '0.7 Gy' (Figure 1H).

Alpha particle-induced DNA damage marker detection and sham irradiation controls

We imaged alpha particle-induced DNA damage markers by confocal and/or widefield immunofluorescence, using: histone $H2AX^{S139p}$ (γH2AX) and the p53-binding protein 1 (53BP1) to demarcate DNA double-strand breaks (DSB) and poly(ADP-ribose) (PAR) to demarcate DNA break-dependent PAR Polymerase (PARP) activity; for a review of these markers, see (3,61). An acute 0.7 Gy dose of particles induced γH2AX, 53BP1 and PAR in 48BR primary human fibroblasts (Figures 1H and 2A; Supplementary Figure S1A). As particles cannot penetrate normal (ml) quantities of aqueous media, our system necessitates a brief media removal (i.e. elevated oxygenation period) as only a thin liquid monolayer remains. Importantly, 'sham' irradiation (media removal, no IR) did not increase detectable DNA damage, showing that the method's conditions are sufficient to minimize dehydration and/or stress (Figure 2A). We verified this using 48BR cells and other common molecular biology cell lines, including WI-38 primary lung fibroblasts, immortalized, normal epithelial-derived RPE-1^{hTERT} cells, A549 lung adenocarcinoma cells and Hela cells (Supplementary Figures S1 and S2).

Alpha particle-induced DSB repair quantification by immunofluorescence microscopy

DSBs induced by sparsely ionizing photons can be measured by scoring γH2AX foci as 'objects' using straightforward methods so sensitive that they are valuable for patient radiosensitivity diagnosis (4,62). However, direct object counting has less value for densely ionizing particles, as

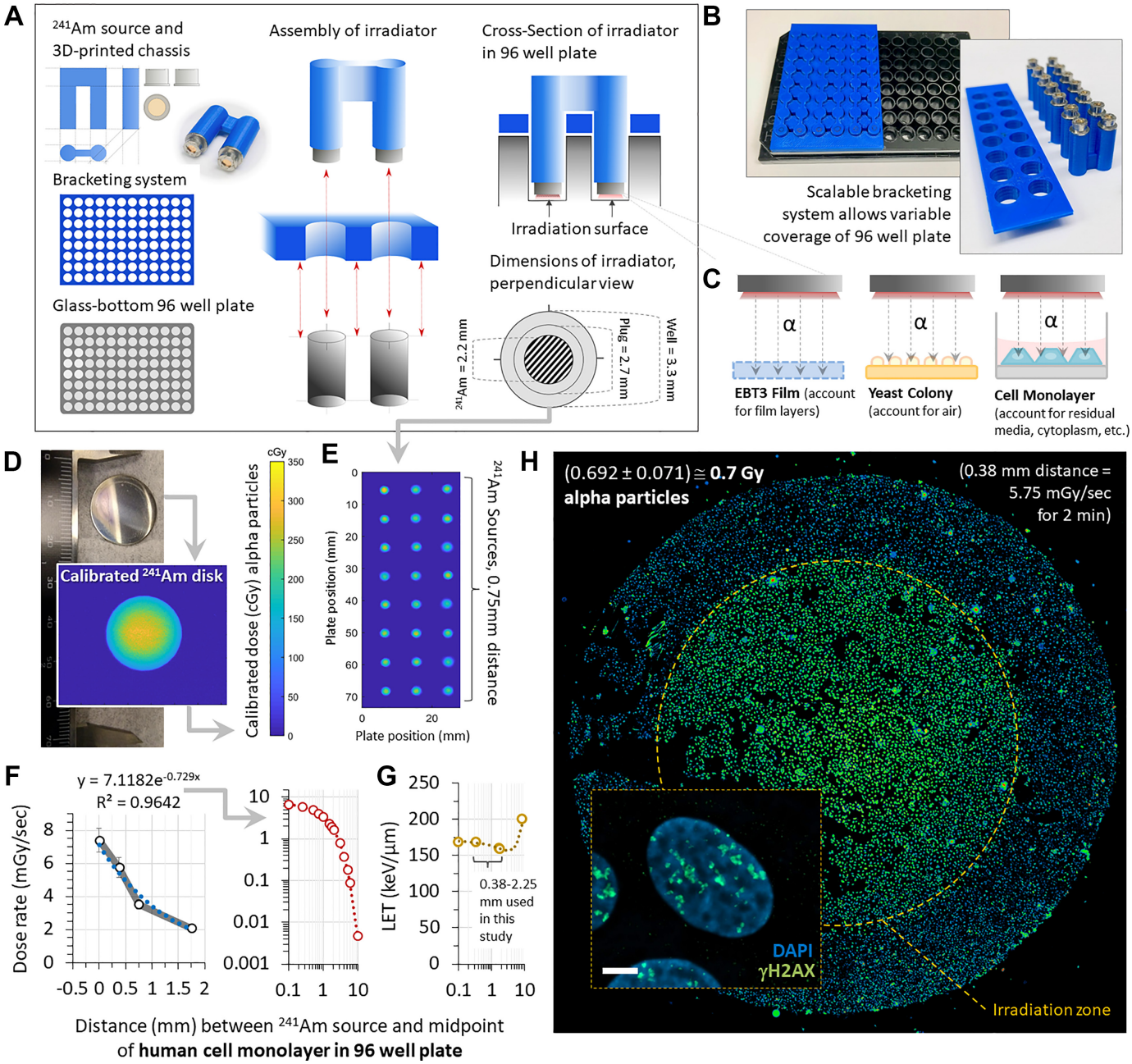

Figure 1. Design and Dosimetry of High-Throughput Alpha Particle Irradiator. Panel (**A**): Schematic and dimensions of ^{241}Am sources with plug-and-bracket chassis compatible with 96-well plate glass bottom dishes. Panel (**B**): Photos of irradiator brackets with 96-well plate. Panel (**C**): Cartoon depictions of three irradiation modalities used in this study. Panel (**D**): Photo shows the calibrated ^{241}Am disk used to ascertain precise dosimetry via EBT3 film. Panel (**E**): Sample 2D dose distribution image of alpha particle-compatible EBT3 film exposed to ^{241}Am sources. Panel (**F**): Dose rate (mGy/s) for human fibroblasts in a 96-well plate, as a function of ^{241}Am source distance from well surface. Data on left represent $n = 3$ independent experimental repeats of 18–40 exposures per experiment, data on right extrapolates out dose rates to 10 mm; error bars = SD. Panel (**G**): The LET (keV/μm) of particle IR as a function of well to surface distance. Panel (**H**): Tiled immunofluorescence image of 48BR fibroblast cells from one entire well of a 96 well plate exposed to 0.692 ± 0.071 Gy alpha particles at 5.75 mGy/s and fixed and stained 1 h later. Cells were stained with γH2AX, with colours representing the red-blue LUT of signal intensity. Orange dashed lines indicate the field of irradiation. Inset image shows a single nuclei of an alpha particle exposed cell stained with γH2AX (green) and DAPI (blue), scale bar = 5 μm.

γH2AX signal converges into clusters and are not distinguishable as single foci representing single lesions (8,9) (Figure 1H). Complicating matters further, measuring γH2AX intensity alone generates a misleading output, as γH2AX intensities per DSB change with time due to chromatin and kinase signalling nuances unrelated to the absolute amount of damage. Cell cycle phase must also be considered, as G_2 cells will display double γH2AX relative to G_0/G_1, due to DNA content changes (62), and so intensity and damage are not strictly linked. These limitations render γH2AX 'total signal' or intensity measures relatively useless, and this is especially important in the case of high LET IR where the alternative (direct object counting) cannot be used. Thus, we set out three conditions for our new particle data compatible approach: (i) it must account for cell cycle and γH2AX per DSB changes over time; (ii) it should be largely automated to enable high-throughput and diminish user bias; and (iii), although accurate and precise for measuring particle-induced DSB repair over time, if applied to photon-induced γH2AX signal, the approach must also produce the well-established photon-induced DSB repair kinetics as calculated using straightforward foci counting, as this will permit researchers to use the method for particle-photon comparisons.

To achieve this, we exposed 48BR fibroblasts to alpha particles or X-ray photons and captured nine *z*-stack images (based on Nyquist sampling optimum) using wide-field epifluorescence microscopy with a 40X air objective (amenable to high-throughput screening) with 5500 nm stack shifts (Figure 2B and Supplementary Figure S1B). Widefield microscopy was used for this high-throughput approach as it has much faster image capture times compared to confocal, whilst still providing sufficient resolution. We note, however, that it is compatible with confocal should users require enhanced resolution for their application. We built an automated protocol involving the TANGO plugin for ImageJ to create an analysis pipeline of structures. TANGO is a free tool based on widely used and freely-available ImageJ and R functionalities. We measured the total number of γH2AX objects per cell over time, observing broadly comparable object induction with 0.7 Gy particles and 2.4 Gy photons (Figure 2C). We then applied the workflow outlined in Figure 2D. Specifically, we determined the mean volume of these γH2AX objects per cell (Supplementary Figure S1C); and normalized their integrated density (i.e. intensity) with their volume (Supplementary Figure S1D). As TANGO counts all detectable objects, including small, background irregularities, it was essential to apply a threshold value to derive a 'legitimate' γH2AX foci or cluster count. This threshold was defined as two standard deviations greater than the smallest Gaussian peak of all object's volume-normalized γH2AX intensity in the unirradiated condition (Supplementary Figure S1E, see 'Materials and Methods' section for details). We then calculated 'temporal correction values' to account for γH2AX signal expansion over time by evaluating mean volume of legitimate γH2AX objects as a function of the total number of objects per cell (Supplementary Figure S1F and G). The integrated DAPI density correlates to total DNA content (63) and is useful to monitor cell cycle staging and/or nuclear size variation. Using this, asynchronously dividing cells were separated into G1, S and G2 populations, displaying anticipated differences in γH2AX object induction (62) (Figure 2E and F).

In short, our principle reported DSB signal value, termed 'refined γH2AX', represents the mean intensity of legitimate γH2AX objects per cell expressed as a function of nuclear size (DAPI volume) and corrected for signal expansion. This refinement allows γH2AX quantification in a computer-automated manner from $>10^3$ cells per experiment, controlling for cell size and phase, and enabling variable IR LET comparisons. Using this in 48BR cells, we observed a linear signal increase with particle dose (0.1–1.0 Gy at 0.35 Gy/min), with $r^2 = 0.936$ indicating that signal correlates closely with dose (Figure 2G). Refined γH2AX signal peaked at 0.5 h for photons and 1 h for particles; by 24 h post IR, <5% photon-induced signal remained, whilst 40% of particle-induced signal persisted (Figure 2H–I). Over 12 h, the DSB repair rate was 4.07 times slower for particles compared photons, with a larger 'slow component' of biphasic DSB repair observable for particle-induced damage (Figure 2J); this fits with understood radiobiology (2,6–10). The method is compatible with other markers such as 53BP1 (Supplementary Figure S1H), and was verified for WI-38, RPE-1^{hTERT}, A549, and Hela cell lines (Supplementary Figure S2A–C).

Repetitive particle irradiation and γH2AX signalling requirements

One of the greatest advantages of this system is convenient and cheap repetitive irradiation for prolonged periods to model impact(s) of steady, but lower dose particle exposure more commonly observed in the environment. To demonstrate this, we exposed 48BR cells to 35–140 mGy particles once per day for 15 consecutive days and compared the refined γH2AX signal to that induced by a single, acute dose of 0.5 or 1.0 Gy particles (Figure 2K). As predicted from data in Figure 2J, 15 days of repetitive particle exposure (even as low as 35 mGy per day) lead to an accumulation of refined γH2AX signal. To visualize the events underlying this in greater detail, we delivered 0.7 Gy per day over a 120 h period to WI-38 primary lung fibroblasts, and harvested cells 1 or 24 h post IR each day, as per the workflow in Figure 3A. Using this, one may observe the progressive increases in refined γH2AX signal each day across a 120 h period (Figure 3B and C).

We next explored compatibility with small molecule testing and genetic screening endpoints in the context of γH2AX signalling, specifically examining the impact of two widely used ATM or DNA-PKcs protein kinase inhibitors (ATMi and DPKi, respectively) (64) and/or DNA-PKcs ablation via CRISPR-Cas9 gene editing (56). As signal expansion is an endpoint for this type of experiment, we removed the final step (#6) from the workflow shown in Figure 2D to generate quantified data. ATMi suppressed particle-induced γH2AX signal intensity and demonstrated significant effects in five distinct cell models (Figure 3D and E). DPKi treatment had a smaller or non-significant effect. DNA-PKcs deletion had a markedly different (and much stronger) impact compared to DPKi treatment, highlighting measurable nuances between small molecule inhibition

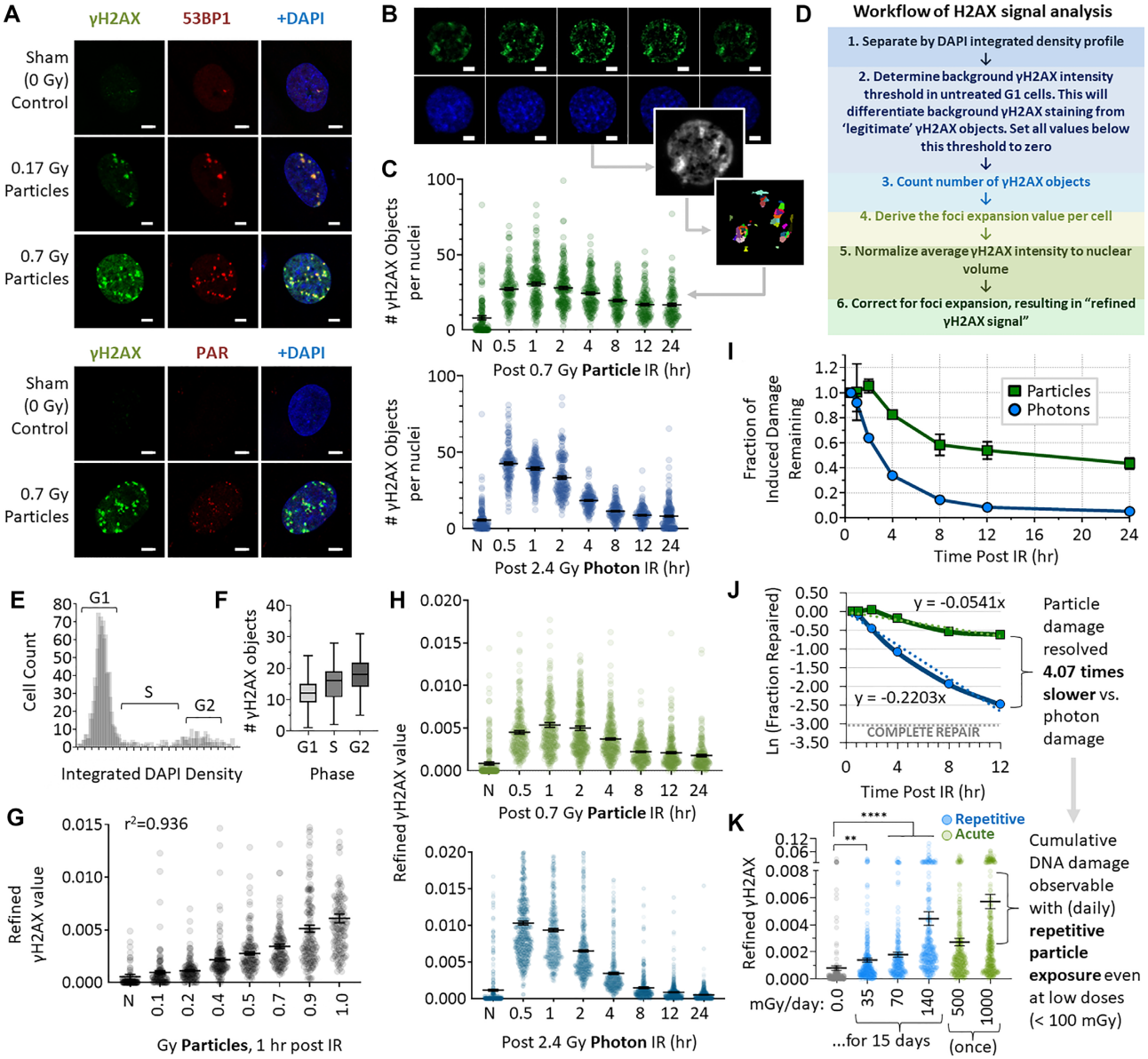

Figure 2. Calculating DNA Double Strand Break Repair Kinetics with Particles versus Photons. All scatter plot dots in this figure are set to 80% transparency to visualize data density, with black bars = mean ± SEM of n = 3. Panel (**A**): 48BR cells were exposed to 0.17 or 0.7 Gy particles or sham irradiated (media removal, no IR) and, 1 h later, fixed, immunostained and imaged using confocal microscopy for γH2AX (green), 53BP1 (red), PAR (red) and/or DAPI (blue) as indicated; scale bars = 2 μm. Panel (**B**): Upper images are representative of five z-stacked images (from the experiment in (A) but imaged using widefield microscopy), with lower images indicating ImageJ/TANGO segmented 3D volume of γH2AX signal and isolated γH2AX objects across the *z*-plane; Scale bars = 5 μm. Panel (**C**): The total number of γH2AX objects per cell for 48BR irradiated with 0.7 Gy particles (dark green dots) or 2.4 Gy photons (dark blue dots) over a 24 h period. Panel (**D**): Our workflow for image analysis generating 'refined γH2AX'. Panel (**E**): The integrated DAPI density of cells in (C) showing cell cycle phase population distribution and differences in γH2AX object number per G1, S or G2 cells using integrated DAPI density, $n = 3$ (1150 cells total). Panel (**F**): Box plot of median and the 25/75th percentiles of data in (E), whiskers represent min/max. Panel (**G**): Refined γH2AX for 48BR irradiated with increasing particle doses and examined 1 h post IR, $n = 3$ (150–500 cells total). Panel (**H**): Refined γH2AX signal for cells from (C), $n = 3$ (150–500 cells total). Panel (**I**): The mean refined γH2AX signal at 0.5 h post IR was set to 1 to plot the fraction of induced damage remaining over time for cells in (C), with particles shown in green and photons in blue. Panel (**J**): Data from (I) was Ln-transformed to plot DNA repair kinetics. Panel (**K**): 48BR cells were repetitively exposed to 35, 70 or 140 mGy particle IR once per day for 15 days (blue), or a one-time (acute) dose of 500 or 1000 mGy particle IR (green). Repetitively irradiated cells were harvested 24 h after the final dose, whilst acutely irradiated cells were harvested 1 h post IR. All cells were then fixed, stained and imaged together, generating refined γH2AX signal; $n = 3$ (1700 cells total per condition). ** = statistically significant (<0.01); **** = statistically significant (<0.0001).

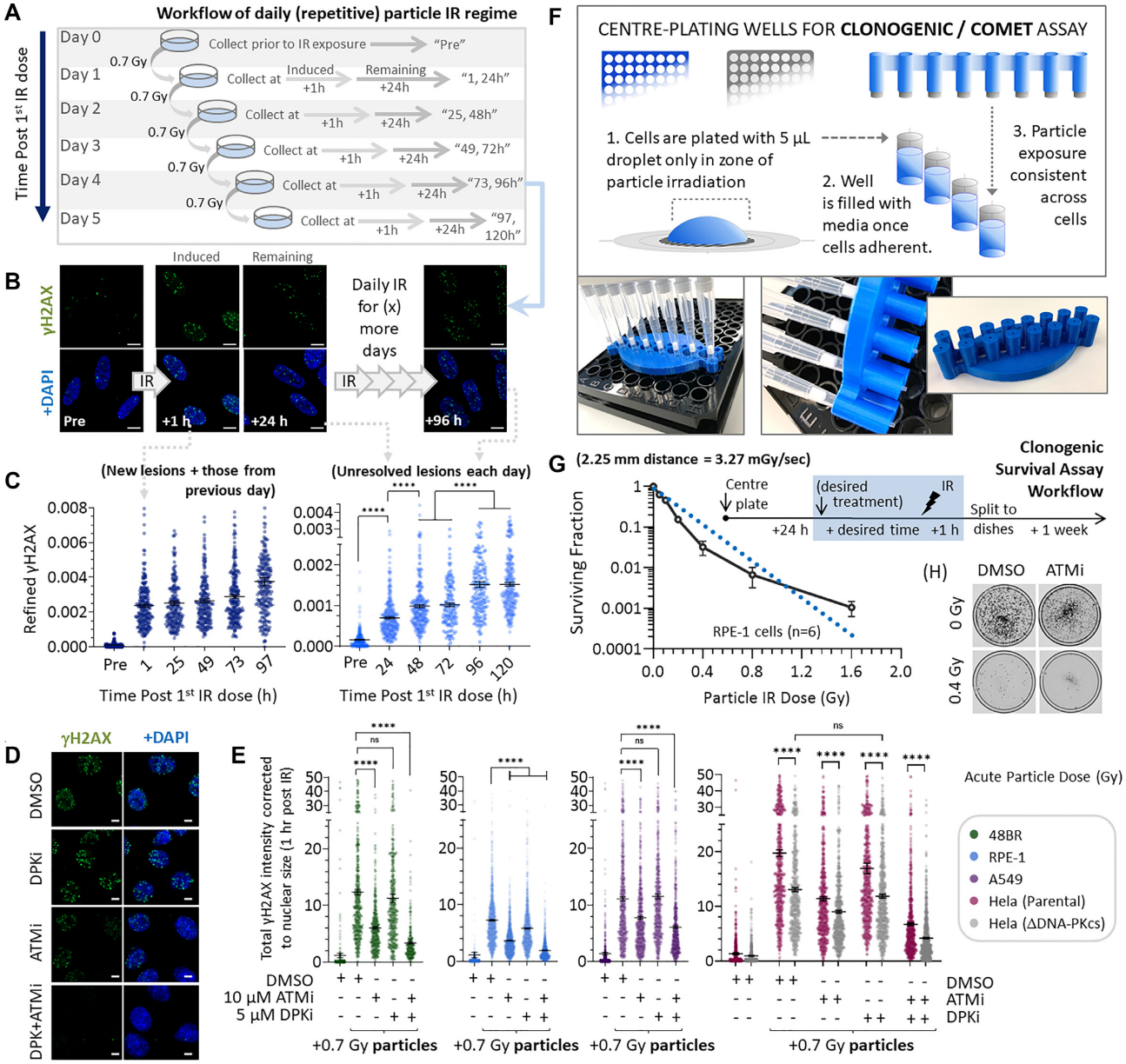

Figure 3. Repetitive Particle Irradiation, Signaling Dependencies and Clonogenic Survival. Panel (**A**): Schematic of repetitive particle IR to monitor accumulating damage. Panel (**B**): WI-38 primary lung fibroblasts were exposed to 0.7 Gy per day for 5 consecutive days as in (A). At indicated times post IR, cells were immunostained for γH2AX (green) and DAPI (blue). Scale bars = 10 μm. Panel (**C**): Cells from (A-B) were quantified for refined γH2AX signal. Dark blue indicates 1 h post IR time points, whilst light blue indicates 24 h post IR; n = 3, 1300 cells per condition. Panel (**D**): 48BR cells were treated with 10 μM ATMi and/or 5 μM DPKi (or an equivalent volume of DMSO) for 0.5 h prior to IR with 0.7 Gy particles; cells were fixed 1h later and immunostained for γH2AX and DAPI (scale bars on all images = 5 μm). Panel (**E**): The experiment in (D) was reproduced for five cell lines: 48BR primary fibroblasts, hTERT-immortalized (normal-derived) RPE-1 cells, A549 lung adenocarcinoma cells, Hela cells and Hela cells gene-edited (via CRISPR-Cas9) to ablate DNA-PKcs expression. In all cases, γH2AX signal intensity was corrected for overall nuclear (DAPI) volume and analyzed for n = 3 experiments (200–250 cells total). Panel (**F**): Schematic for centre-well plating of cells to ensure even particle radiation dose distribution, with photos of custom printed centre-plating guide for multi-channel pipetting. Panel (**G**): Quantified clonogenic survival data (n = 6) for centre-plated RPE1 cells treated with up to 1.6 Gy of acutely-delivered particle IR using a 2.25 mm IR source-to-well distance. Inset shows the workflow for clonogenic survival assay using particles. Panel (**H**): Representative images of plates of RPE1 cells treated for 2 hr with 10 μM ATMi before being assayed for clonogenic potential following particle IR using the workflow in (G). ns = non-significant (>0.05); **** = statistically significant (<0.0001).

and deletion models. Combined ATMi and either DPKi treatment or DNA-PKcs deletion, was additive, ablating the majority of γH2AX signalling in most cell models (Figure 3E). This fits with understood redundancies between ATM and DNA-PKcs for photon-induced γH2AX formation (64).

Monitoring alpha particle-induced effects on clonogenic survival and viability

Quantitative measurements of cell viability and clonogenic survival are other important radiobiology endpoints. In these cases, it is essential that all cells are irradiated essentially equally, as (unlike microscopy) it is not practical to measure only cells directly under the irradiation field. To ensure this, we developed a centre-plating technique (Figure 3F) whereby a custom (3D-printed) multi-well pipette guide ensures that cells in 5 μl droplets are plated in the exact centre of 96-well plate wells, allowed to adhere, then grown so that cell monolayers are only present within the irradiation zone and well away from the periphery and residual media meniscus (Supplementary Figure S2D). We then performed classic clonogenic survival assays using RPE-1 cells and a single, acute dose of particles delivered at 0.4 Gy per minute at a height of 2.25 mm above the cell monolayer, as per the workflow in Figure 3G. We observed progressive loss in clonogenic potential with increasing dose, with 0.1–1% cell survival after 0.8–1.6 Gy particles. To demonstrate compatibility with small molecule screening, we treated cells with 10 μM ATMi for 1 h prior to IR, and found ATMi treatment demonstrated a degree of radiosensitization (Figure 3H), fitting with established literature. We also examined the utility of cell viability assays that use colorimetry to monitor the live-cell specific metabolism of the resazurin dye Alamar Blue. Such assays are much faster, but considerably less sensitive than clonogenic survival assays. 48BR cells were centre-well plated, exposed to particles, allowed to recover 24 h, incubated with Alamar Blue for 8 h and assessed by automated plate-reader imaging. Staurosporine served as a cell death positive control. Particles induced a dose-dependent decrease in viability, with 20–40% loss after 2.8–11 Gy, but no significant effect after 1.4 Gy (Supplementary Figure S2E). This demonstrates compatibility with viability assays, although these are much less sensitive compared to clonogenic survival endpoints.

Alpha particle-induced DNA damage quantification by alkaline comet assay

Comet assays are a physical, single-cell readout of DNA breakage that measures damage and repair heterogeneity in a population, and are very important endpoints in the DNA repair field (59). Neutral pH assays detect DSBs, whilst alkaline assays detect both DSBs and DNA single strand breaks (SSBs), and are compatible with high-throughput modalities (65). Historically, comet assays have been used only rarely with alpha particles (<20 studies in PubMed literature), presumably due to challenges in irradiating cells in suspension, a necessary step in the most commonly used, standard protocols. As neutral assays require ≥30 Gy doses (62), we used lower-dose compatible alkaline conditions per the workflow in Figure 4A. Centre-plated 48BR cells were irradiated whilst adherent (essential for this method) and processed via standard comet protocols (58,59,62). We delivered particles or photons in either cold buffer conditions (precluding repair during IR) or in warm media (i.e. same approach as γH2AX analysis), wherein cold buffer or warm media are returned to cells for 2 min in between eight fractions. Doses were chosen to induce comparable refined γH2AX signals based on our findings in Figure 2, equating to 5.5 Gy particles and 6.4 Gy photons. Particles induced significant comet tails that resolved over time, validating our method for physical DNA break applications (Figure 4B). A modest increase in particle-induced signal was observed in warm media versus cold buffer, and we speculate this is either attributable to heat-labile sites (66) or ongoing base lesion repair pathways that generate SSBs as intermediates (67). In cold buffer, 6.4 Gy photons induced an alkaline tail moment 5.5 times greater than was induced in media, likely due to ongoing SSB repair during irradiation in warm media conditions (Figure 4C). In cold buffer, particles induced a 4.5 times smaller tail moment compared to photons, suggesting a much smaller burden of induced SSBs (Figure 4D). Particle-induced damage was repaired more slowly over the irradiation period compared to photons, (once again) being 4.07 times slower when IR was delivered in media (Figures 2J and 4E).

Monitoring alpha particle-induced effects by oxidative stress assay

The reproducible particle versus photon DNA repair kinetic trends observed using γH2AX and comet assays adds confidence to the method, and suggests particles generate more DSBs per SSBs per dose relative to photons. We speculated (as others have) (68) that this is due to greater direct DNA ionization and/or less reactive oxygen species (ROS) generation/oxidative stress. To interrogate this further, we treated cells in media with a PARP inhibitor (PARPi) or DMSO before irradiation. DMSO is a mild antioxidant and suppresses SSB-generating ROS generated by IR-induced water radiolysis. PARPi precludes SSB repair, but generally does not impinge on DSB repair in wild-type cells. Whilst photon-induced alkaline tail moments (i.e. SSB induction) were suppressed by DMSO and increased by PARPi, these compounds had no significant impact on particle-induced damage (Figure 4F). This strengthens the notion that alpha particles produce more harder-to-repair DSBs and/or complex SSBs relative to photons, and less fast-repairing, sparse damage. To see whether our system was amenable to interrogate ROS production directly, we applied a widely used, high-throughput oxidative stress assay as per the workflow in Figure 4G. Using this, we observed significant ROS production in 48BR and RPE-1 cells following acute photon or H_2O_2 exposure (in warm media), but not after particles at doses that produce broadly equivalent refined γH2AX (Figure 4H). To explore this further, we incubated cells with antioxidant radioprotectants (agents highly sought after for health protection (69)) including epicatechin, myricetin and the Bowman–Birk inhibitor (BBI) peptide (70–72). Whilst the small molecules all suppressed photon-induced γH2AX foci and/or alkaline comet tails, we saw no significant effects

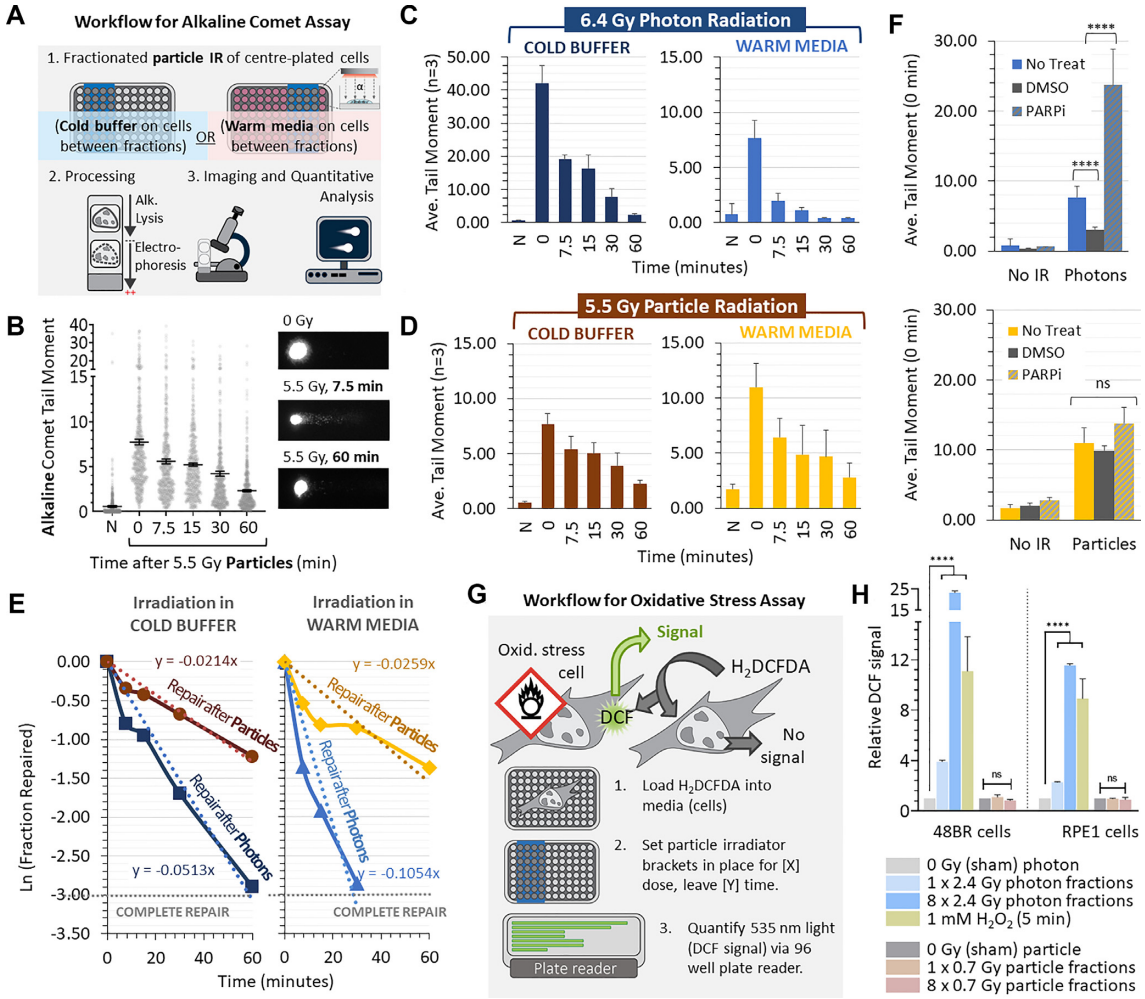

Figure 4. Alpha Particle Irradiation for Alkaline Comet Assay. Panel (**A**): Workflow of particle IR of centre-plated cells for comet assay. Panel (**B**): Raw data from three independent experiments showing distribution of alkaline tail moments over time in 48BR primary human fibroblasts exposed to 5.5 Gy particle radiation in cold HBSS buffer. Dots are set to 80% transparency to visualize data density, with bars indicating the mean ± SEM and with n = 3 (600–1000 cells total) experiments layered on top of one another. To right are representative images of particle-induced comet tails. Panel (**C**): Average alkaline comet tail moments of 48BR cells exposed to photon radiation either in cold HBSS buffer (dark blue bars) precluding ongoing DNA repair during irradiation, or in warm media (light blue bars) allowing ongoing repair. Doses were fractionated into eight 0.8 Gy doses to replicate conditions used during particle irradiation. Error bars = SEM based on n = 3 experiments (600–800 cells total). Panel (**D**): Average alkaline comet tail moments for 48BR cells exposed to particle radiation either in cold HBSS buffer (dark orange bars, precluding ongoing DNA repair during irradiation) or in warm media (yellow bars, allowing ongoing repair). Doses were fractionated into eight x 0.7 Gy. Error bars = SEM based on n = 3 experiments (600–800 cells total). Panel (**E**): Average alkaline comet tail data from (C and D) were expressed as Ln-transformed relative fraction of induced (0 min) damage remaining over time. Panel (**F**): 48BR cells were treated ± 0.05% (v/v) DMSO or 2.5 μM PARPi for 1 h before being irradiated as in (C and D) and harvested immediately (0 min post IR). Blue bars = photon radiation. Yellow bars = particle radiation. Error bars = SEM. Panel (**G**): Workflow for monitoring oxidative stress. Panel (**H**): 48BR cells were exposed to 1 or 8 fractions of photon or particle IR (as indicated) and analyzed immediately (i.e. in <5 min) for oxidative stress as in (G). A positive control for oxidative stress was a 5 minute exposure to 1 mM H_2O_2 (added to media). ns = non-significant (>0.05); **** = statistically significant (<0.0001).

with particles (Supplementary Figure S3A–D). This adds to the existing idea (68) that particles rely less on ROS generation to elicit DNA damage and affirms the utility of our method for small molecule testing or screening (even if the outcome is to eliminate candidate compounds).

Monitoring alpha particle-induced effects using *S. cerevisiae* as model system

Fast and pliable genetic model systems such as *S. cerevisiae* use cell viability and growth measures to monitor toxin effects. Using 3D printing, we designed and printed a chassis compatible with yeast growth media plates with a 1.9 Gy/min particle dose rate (Figure 4A and B). Yeast are orders of magnitude more resistant to IR, with kGy doses needed to observe >90% loss of yeast survival (73), versus only low Gy in human cells (23). Hence, Gy doses to yeast are equivalent to mGy doses in humans and thus represent 'low doses'. Also useful is that yeast survives on solid media lacking aqueous barriers to irradiation, thus making low dose, chronic exposure experiments straightforward to conduct. Using logarithmically growing *S. cerevisiae* cultures at 8×10^7 cells/ml, we performed serial dilutions and plated 10^5–10^2 cells, exposed them to 0–2.7 kGy particles at

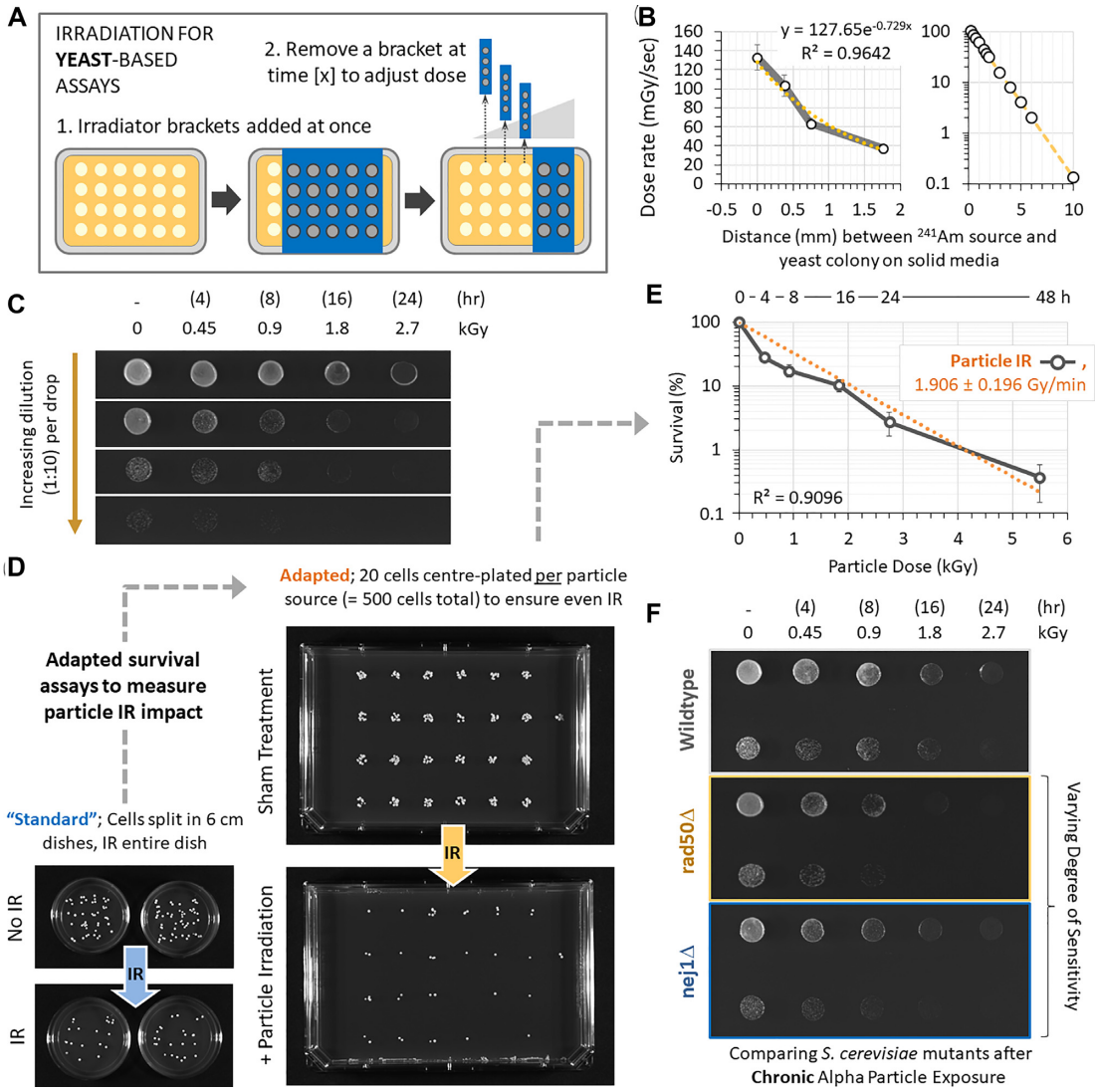

Figure 5. Alpha Particle Irradiation in Yeast Cell Model Systems. Panel (**A**): Schematic for irradiating yeast cells on solid media with particle radiation. Panel (**B**): Dose rate (mGy/sec) calculated for *S. cerevisiae* irradiation on solid media, as a function of ^{241}Am source distance from colony surface. Data derived from calculations in Figure 1D–F. Panel (**C**): Drop assays with increasing chronic particle radiation (exposures 4–24 h, doses as indicated). In each panel, wildtype was plated at a density from 8×10^4 to 8×10^7 cells/ml (top to bottom). Panel (**D**): Representative photos of quantitative yeast survival assays with 'standard' (blue) methods, versus our adapted (orange) method compatible with high-throughput particle IR. Panel (**E**): Quantified cell survival data after exposure to increasing particle IR doses (0–5.5 kGy) using the method shown in (D). Error bars = SEM based on $n = 3$ experiments. Panel (**F**): Drop assays with increasing chronic particle IR with wildtype, *rad50Δ* or *nej1Δ* mutant cells.

room temperature, followed by a 10 h recovery at 30°C. Cell survival decreased with increasing IR dose, validating our protocol (Figure 5C). For quantitative experiments, yeast cells are plated at a density (~500 cells) compatible with direct enumeration and then exposed to chronic particle IR (Figure 5D). Twenty individual yeast cells were plated directly below each particle IR source in a plate, then subjected to IR or sham control. This quantitative readout allows a wide range of dose responses (Figure 5E). Finally, as a proof of principle of genetic screening, we examined *S. cerevisiae* mutants impaired for distinct DSB repair components. These included NEJ1 (yeast equivalent of human XLF) involved in non-homologous end-joining mediated DSB ligation, and RAD50 that enables 5′ DNA resection at DSBs. Both *rad50Δ* and *nej1Δ* showed a degree of particle sensitivity (Figure 5F). Collectively, this demonstrates the exciting potential of this new approach for a wide variety of screening purposes.

DISCUSSION

The technology we describe here represents an innovative, potentially game-changing approach for the high-throughput study of the effects of alpha particles in the biological context. The key advantage of this method is that it enables researchers to perform low dose, long term, repetitive exposure particle irradiation experiments on a scale and in a way that was impractical with previous methodologies; that is, in a high capacity manner for relatively low costs. It also avoids the need to grow cells on delicate

ultra-thin plastic film that can modify or complicate cell growth conditions. In terms of limitations, the need to remove media (from mammalian cells) during IR is an unavoidable inconvenience and, although we were not able to detect significant increases in DSB or SSBs for the typically 2 min of media removal we employed, should be taken into consideration by users. It is worth noting this limitation does not apply to yeast model systems. In the broader context of high LET IR research, this method matches previous techniques (9,11–17), in that it also avoids the need to access particle accelerators—an inherently expensive approach that is often limited in availability due to logistical challenges. Finally, this method permits researchers to use the same IR platform with multiple model organisms, including mammalian cells and yeast, and to apply high-throughput modalities across a much wider variety of experimental endpoints that have been reported previously for a given benchtop alpha particle irradiator. Thus, this method may help to alleviate the research bottleneck that has, so far, restricted advances in particle IR research compared to photons—particularly as it relates to low dose, long term repetitive IR exposure which is most relevant to human environmental alpha particle exposure via radon (31).

Our method is useful to monitor the known differences between alpha particle and photons that must be taken into account when studying these radiation types in relation to one another (8–10,19,23,27). For an equivalent dose relative to photons, particles generate: (i) harder/slower-to-repair lesions, which (in addition to differing lesion complexities) is possibly consistent with higher LET IR 'relying' less on ROS generation to produce DNA damage; (ii) smaller alkaline comet tail moments (i.e. less ROS-induced SSBs) under cold buffer, no-repair conditions, (iii) similar tail moments under warm media, active repair conditions and (iv) DNA damage not significantly influenced by antioxidants or PARP inhibitors. There are also differences in DSB-induced signal expansion over time between particle and photons that require distinct correction values in order to compare data from photon and particles in an informative manner. We stress that failure to account for this may generate otherwise avoidable artefacts in repair kinetics. Future research, enabled by the method(s) we describe here, will help clarify the etiology of these phenomena.

Finally, the prospect of high throughput screening a variety of genetic systems and/or small molecules in the context of alpha particle irradiation effects is very compelling. Experiments using yeast have been enormously impactful to our knowledge of biological pathways involved in high dose, acute photon radiation effects, and almost certainly will be impactful to our understanding of high or low dose, acute, repetitive or chronic effects of particle exposure. Now that gene-edited cell lines are widely available to perform such experiments in the human context, we anticipate a faster, deeper understanding of how genetic and epigenetic differences influence disease susceptibility in the particle context. Similarly, high content screening may hold potential for discovery of novel alpha particle exposure-specific radio-protectants, radio-sensitizers and potential drugs for disease treatment. This has major implications to developing solutions for particle-associated pathologies, wherein chronic, low dose particle bombardment is disease-causing, but for which we are only starting to understand age-associated biomarkers, genetic susceptibilities and exposure prevention measures.

DATA AVAILABILITY

The 3D printing design files and R-markdown code files generated during the current study are freely available by email request to the corresponding author. The software for viewing 3D print files are Fusion 360 from Autodesk and Sketchup. R-markdown code files are viewed using R-Studio. All software is either free with open source licenses or have free trials.

SUPPLEMENTARY DATA

Supplementary Data are available at NAR Online.

ACKNOWLEDGEMENTS

We would like to thank University of Calgary Radiation Safety officers for helpful advice, Dr Susan Lees-Miller (University of Calgary) for providing ΔDNA-PKcs Hela cells (and parental controls), Dr Raphael Galea at the Ionizing Radiation Standards division of the National Research Council of Canada for providing calibrated ^{241}Am sources, and Dr Anne Vaahtokari of the Charbonneau Institute Microscopy Facility for imaging assistance. A.A.G. and F.K.T.S. conceived and designed the original study and, alongside N.D.B., D.D.P. and J.M.D., contributed to all figures. N.D.B. is co-supervised by A.A.G. and J.A. Chan. J.M.D. performed yeast experiments in Figure 5 together with J.A. Cobb. T.W. in the lab of DRB assisted with Figure 3A–C. J.E.J. contributed to Supplementary Figure S2 and preliminary validation of particle irradiator design. H.M., G.P. and N.P.P. performed IR dosimetry analysis in Figure 1 and supported all X-ray photon irradiation experiments. All authors contributed to manuscript preparation.

FUNDING

Daniel Family Foundation Scholarship in Cancer Research (to FKTS); Vanier Canada Graduate Scholarship (to N.D.B.); Cumming School of Medicine Graduate Scholarship (to N.D.B.); Alberta Innovates – Health Solutions Graduate Scholarship (to N.D.B); Izaak Walton Killam Pre-Doctoral Scholarship (to N.D.B.); NSERC Canada Graduate Scholarship (to D.D.P.); Queen Elizabeth II Graduate Scholarship (to D.D.P), an Achievers in Medical Science Doctoral Scholarship (to D.D.P) and the Rejeanne Taylor Research Prize (to D.D.P); Cumming School of Medicine Doctoral Scholarship (to J.M.D.); Alberta Cancer Foundation Clinical Fellowship (to H.M.); Canadian Institutes of Health Research (to J.A.Cobb) [CIHR, MOP-82763, MOP-137062]; National Sciences and Engineering Research Council of Canada (to J.A.Cobb) [NSERC, 418122]; CIHR (to J.A. Chan); Canadian Cancer Society [703917 to D.R.B.]; Canada Research Chair for Radiation Exposure Disease (to A.A.G.); CIHR Funding Reference Number #153121 (to A.A.G.); NSERC 2017-04847 (to A.A.G.); National Chronic Fatigue Immune Dysfunction Syndrome Foundation (to A.A.G). Funding for open access was from CIHR #153121 (to A.A.G).

Conflict of interest statement. None declared.

REFERENCES

1. Jeggo,P.A., Pearl,L.H. and Carr,A.M. (2016) DNA repair, genome stability and cancer: a historical perspective. *Nat. Rev. Cancer*, **16**, 35–42.
2. Pearson,D.D., Anikin,A. and Goodarzi,A.A. (2016) Environmental sources of ionizing radiation and their health consequences. In: *Genome Stability*. Elsevier, p. 712.
3. Goodarzi,A.A. and Jeggo,P.A. (2013) The repair and signaling responses to DNA double-strand breaks. *Adv. Genet.*, **82**, 1–45.
4. Goodarzi,A.A. and Jeggo,P.A. (2012) Irradiation induced foci (IRIF) as a biomarker for radiosensitivity. *Mutat. Res.*, **736**, 39–47.
5. O'Connor,M.J. (2015) Targeting the DNA damage response in cancer. *Mol. Cell*, **60**, 547–560.
6. Okayasu,R. (2012) Repair of DNA damage induced by accelerated heavy ions–a mini review. *Int. J. Cancer*, **130**, 991–1000.
7. Mladenov,E., Saha,J. and Iliakis,G. (2018) Processing-challenges generated by clusters of DNA double-strand breaks underpin increased effectiveness of high-LET radiation and chromothripsis. *Adv. Exp. Med. Biol.*, **1044**, 149–168.
8. Nakajima,N.I., Brunton,H., Watanabe,R., Shrikhande,A., Hirayama,R., Matsufuji,N., Fujimori,A., Murakami,T., Okayasu,R., Jeggo,P. *et al.* (2013) Visualisation of gammaH2AX foci caused by heavy ion particle traversal; distinction between core track versus non-track damage. *PLoS One*, **8**, e70107.
9. Stap,J., Krawczyk,P.M., Van Oven,C.H., Barendsen,G.W., Essers,J., Kanaar,R. and Aten,J.A. (2008) Induction of linear tracks of DNA double-strand breaks by alpha-particle irradiation of cells. *Nat. Methods*, **5**, 261–266.
10. Miller,R.C., Randers-Pehrson,G., Geard,C.R., Hall,E.J. and Brenner,D.J. (1999) The oncogenic transforming potential of the passage of single alpha particles through mammalian cell nuclei. *Proc. Natl. Acad. Sci. U. S. A.*, **96**, 19–22.
11. Esposito,G., Antonelli,F., Belli,M., Campa,A., Simone,G., Sorrentino,E. and Tabocchini,M.A. (2009) An alpha-particle irradiator for radiobiological research and its implementation for bystander effect studies. *Radiat. Res.*, **172**, 632–642.
12. Nawrocki,T., Tritt,T.C., Neti,P., Rosen,A.S., Dondapati,A.R. and Howell,R.W. (2018) Design and testing of a microcontroller that enables alpha particle irradiators to deliver complex dose rate patterns. *Phys. Med. Biol.*, **63**, 245022.
13. M,V.J., Shinde,S.G., S,S.K., Ali,M., Vasumathy,R., Kumar,A., Kolekar,R., Kumar,M., Nema,P., Bhagwat,P.V. *et al.* (2013) Dosimetry and radiobiological studies of automated alpha-particle irradiator. *J. Environ. Pathol. Toxicol. Oncol.*, **32**, 263–273.
14. Soyland,C., Hassfjell,S.P. and Steen,H.B. (2000) A new alpha-particle irradiator with absolute dosimetric determination. *Radiat. Res.*, **153**, 9–15.
15. Metting,N.F., Koehler,A.M., Nagasawa,H., Nelson,J.M. and Little,J.B. (1995) Design of a benchtop alpha particle irradiator. *Health Phys.*, **68**, 710–715.
16. Lee,K.M., Lee,U.S. and Kim,E.H. (2016) A practical alpha particle irradiator for studying internal alpha particle exposure. *Appl. Radiat. Isot.*, **115**, 304–311.
17. Roobol,S.J., Kouwenberg,J.J.M., Denkova,A.G., Kanaar,R. and Essers,J. (2019) Large field alpha irradiation setup for radiobiological experiments. *Methods Protoc*, **2**, 75.
18. UNSCEAR (2000) In: *Sources and Effects of Ionizing radiation*. United Nations, NY.
19. Moore,S., Stanley,F.K. and Goodarzi,A.A. (2014) The repair of environmentally relevant DNA double strand breaks caused by high linear energy transfer irradiation–no simple task. *DNA Repair (Amst.)*, **17**, 64–73.
20. McLean,A.R., Adlen,E.K., Cardis,E., Elliott,A., Goodhead,D.T., Harms-Ringdahl,M., Hendry,J.H., Hoskin,P., Jeggo,P.A., Mackay,D.J.C. *et al.* (2017) A restatement of the natural science evidence base concerning the health effects of low-level ionizing radiation. *Proc. Biol. Sci.*, **284**, 20171070.
21. Mothersill,C., Abend,M., Brechignac,F., Copplestone,D., Geras'kin,S., Goodman,J., Horemans,N., Jeggo,P., McBrideh,W., Mousseau,T.A. *et al.* (2019) The tubercular badger and the uncertain curve:- The need for a multiple stressor approach in environmental radiation protection. *Environ. Res.*, **168**, 130–140.
22. Sridharan,D.M., Whalen,M.K., Almendrala,D., Cucinotta,F.A., Kawahara,M., Yannone,S.M. and Pluth,J.M. (2012) Increased Artemis levels confer radioresistance to both high and low LET radiation exposures. *Radiat. Oncol.*, **7**, 96.
23. Riballo,E., Kuhne,M., Rief,N., Doherty,A., Smith,G.C., Recio,M.J., Reis,C., Dahm,K., Fricke,A., Krempler,A. *et al.* (2004) A pathway of double-strand break rejoining dependent upon ATM, Artemis, and proteins locating to gamma-H2AX foci. *Mol. Cell*, **16**, 715–724.
24. Jefferson,R.D., Goans,R.E., Blain,P.G. and Thomas,S.H. (2009) Diagnosis and treatment of polonium poisoning. *Clin. Toxicol. (Phila)*, **47**, 379–392.
25. Soto,J., Sainz,C., Gonzalez-Lamuno,D. and Cos,S. (2006) Low doses of alpha particle irradiation modify the expression of genes regulating apoptosis in human MCF-7 breast cancer cells. *Oncol. Rep.*, **15**, 577–581.
26. Leatherbarrow,E.L., Harper,J.V., Cucinotta,F.A. and O'Neill,P. (2006) Induction and quantification of gamma-H2AX foci following low and high LET-irradiation. *Int. J. Radiat. Biol.*, **82**, 111–118.
27. Aten,J.A., Stap,J., Krawczyk,P.M., van Oven,C.H., Hoebe,R.A., Essers,J. and Kanaar,R. (2004) Dynamics of DNA double-strand breaks revealed by clustering of damaged chromosome domains. *Science*, **303**, 92–95.
28. Hagiwara,Y., Oike,T., Niimi,A., Yamauchi,M., Sato,H., Limsirichaikul,S., Held,K.D., Nakano,T. and Shibata,A. (2019) Clustered DNA double-strand break formation and the repair pathway following heavy-ion irradiation. *J. Radiat. Res.*, **60**, 69–79.
29. Hei,T.K., Wu,L.J., Liu,S.X., Vannais,D., Waldren,C.A. and Randers-Pehrson,G. (1997) Mutagenic effects of a single and an exact number of alpha particles in mammalian cells. *Proc. Natl. Acad. Sci. U. S. A.*, **94**, 3765–3770.
30. ICPR (2007) The 2007 recommendations of the international commission on radiological protection. ICRP publication 103. *Ann. ICRP*, **37**, 1–332.
31. Stanley,F.K.T., Irvine,J.L., Jacques,W.R., Salgia,S.R., Innes,D.G., Winquist,B.D., Torr,D., Brenner,D.R. and Goodarzi,A.A. (2019) Radon exposure is rising steadily within the modern North American residential environment, and is increasingly uniform across seasons. *Sci. Rep.*, **9**, 18472.
32. Stanley,F.K., Zarezadeh,S., Dumais,C.D., Dumais,K., MacQueen,R., Clement,F. and Goodarzi,A.A. (2017) Comprehensive survey of household radon gas levels and risk factors in southern Alberta. *CMAJ Open*, **5**, E255–E264.
33. Gaskin,J., Coyle,D., Whyte,J. and Krewksi,D. (2018) Global estimate of lung cancer mortality attributable to residential radon. *Environ. Health Perspect.*, **126**, 057009.
34. Kim,S.H., Hwang,W.J., Cho,J.S. and Kang,D.R. (2016) Attributable risk of lung cancer deaths due to indoor radon exposure. *Ann. Occup. Environ. Med.*, **28**, 8.
35. Milner,J., Shrubsole,C., Das,P., Jones,B., Ridley,I., Chalabi,Z., Hamilton,I., Armstrong,B., Davies,M. and Wilkinson,P. (2014) Home energy efficiency and radon related risk of lung cancer: modelling study. *Brit. Med. J.*, **348**, f7493.
36. Lobrich,M. and Jeggo,P.A. (2019) Hazards of human spaceflight. *Science*, **364**, 127–128.
37. Garrett-Bakelman,F.E., Darshi,M., Green,S.J., Gur,R.C., Lin,L., Macias,B.R., McKenna,M.J., Meydan,C., Mishra,T., Nasrini,J. *et al.* (2019) The NASA Twins Study: A multidimensional analysis of a year-long human spaceflight. *Science*, **364**, eaau8650.
38. Loganovsky,K., Perchuk,I. and Marazziti,D. (2015) Workers on transformation of the shelter object of the Chernobyl nuclear power plant into an ecologically-safe system show qEEG abnormalities and cognitive dysfunctions: A follow-up study. *World J. Biol. Psychiatry*, **17**, 600–607.
39. Thomas,H.V., Stimpson,N.J., Weightman,A.L., Dunstan,F. and Lewis,G. (2006) Systematic review of multi-symptom conditions in Gulf War veterans. *Psychol. Med.*, **36**, 735–747.
40. Ranjith,G. (2005) Epidemiology of chronic fatigue syndrome. *Occup. Med. (Lond.)*, **55**, 13–19.
41. Allen,C., Borak,T.B., Tsujii,H. and Nickoloff,J.A. (2011) Heavy charged particle radiobiology: using enhanced biological effectiveness and improved beam focusing to advance cancer therapy. *Mutat. Res.*, **711**, 150–157.

42. Devic,S., Seuntjens,J., Sham,E., Podgorsak,E.B., Schmidtlein,C.R., Kirov,A.S. and Soares,C.G. (2005) Precise radiochromic film dosimetry using a flat-bed document scanner. *Med. Phys.*, **32**, 2245–2253.
43. Devic,S. (2011) Radiochromic film dosimetry: past, present, and future. *Phys. Med.*, **27**, 122–134.
44. Reinhardt,S., Hillbrand,M., Wilkens,J.J. and Assmann,W. (2012) Comparison of Gafchromic EBT2 and EBT3 films for clinical photon and proton beams. *Med. Phys.*, **39**, 5257–5262.
45. Lewis,D., Micke,A., Yu,X. and Chan,M.F. (2012) An efficient protocol for radiochromic film dosimetry combining calibration and measurement in a single scan. *Med. Phys.*, **39**, 6339–6350.
46. Berger,M.J., Coursey,J.S., Zucker,M.A. and Chang,J. (2005) In: *ESTAR, PSTAR, and ASTAR: Computer Programs for Calculating Stopping-Power and Range Tables for Electrons, Protons, and Helium Ions*. 1.2.3 edn, National Institute of Standards and Technology, Gaithersburg, MD.
47. Morrison,H., Menon,G. and Sloboda,R.S. (2014) Radiochromic film calibration for low-energy seed brachytherapy dose measurement. *Med. Phys.*, **41**, 072101.
48. Morrison,H. (2017) University of Alberta.
49. Martisikova,M. and Jakel,O. (2010) Dosimetric properties of Gafchromic EBT films in monoenergetic medical ion beams. *Phys. Med. Biol.*, **55**, 3741–3751.
50. Castriconi,R., Ciocca,M., Mirandola,A., Sini,C., Broggi,S., Schwarz,M., Fracchiolla,F., Martišíková,M., Aricò,G., Mettivier,G. *et al.* (2017) Dose-response of EBT3 radiochromic films to proton and carbon ion clinical beams. *Phys. Med. Biol.*, **62**, 377–393.
51. Vadrucci,M., Esposito,G., Ronsivalle,C., Cherubini,R., Marracino,F., Montereali,R.M., Picardi,L., Piccinini,M., Pimpinella,M., Vincenti,M.A. *et al.* (2015) Calibration of GafChromic EBT3 for absorbed dose measurements in 5 MeV proton beam and (60)Co gamma-rays. *Med. Phys.*, **42**, 4678–4684.
52. Kirby,D., Green,S., Palmans,H., Hugtenburg,R., Wojnecki,C. and Parker,D. (2010) LET dependence of GafChromic films and an ion chamber in low-energy proton dosimetry. *Phys. Med. Biol.*, **55**, 417–433.
53. Werner,C.J. (2017) In: *MCNP Users Manual - Code Version 6.2*. Laboratory, L.A.N., Los Alamos National Laboratory.
54. Noon,A.T., Shibata,A., Rief,N., Lobrich,M., Stewart,G.S., Jeggo,P.A. and Goodarzi,A.A. (2010) 53BP1-dependent robust localized KAP-1 phosphorylation is essential for heterochromatic DNA double-strand break repair. *Nat. Cell Biol.*, **12**, 177–184.
55. Woodbine,L., Brunton,H., Goodarzi,A.A., Shibata,A. and Jeggo,P.A. (2011) Endogenously induced DNA double strand breaks arise in heterochromatic DNA regions and require ataxia telangiectasia mutated and Artemis for their repair. *Nucleic Acids Res.*, **39**, 6986–6997.
56. Douglas,P., Ye,R., Radhamani,S., Cobban,A., Jenkins,N.P., Bartlett,E., Roveredo,J., Kettenbach,A.N. and Lees-Miller,S.P. (2020) Nocodazole-induced expression and phosphorylation of anillin and other mitotic proteins is decreased in DNA-dependent protein kinase catalytic subunit (DNA-PKcs)-deficient cells and rescued by inhibition of the Anaphase Promoting Complex/Cyclosome (APC/C) with proTAME but not apcin. *Mol. Cell. Biol.*, **40**, e00191-19.
57. Sorenson,K.S., Mahaney,B.L., Lees-Miller,S.P. and Cobb,J.A. (2017) The non-homologous end-joining factor Nej1 inhibits resection mediated by Dna2-Sgs1 nuclease-helicase at DNA double strand breaks. *J. Biol. Chem.*, **292**, 14576–14586.
58. Moore,S., Berger,N.D., Luijsterburg,M.S., Piett,C.G., Stanley,F.K.T., Schrader,C.U., Fang,S., Chan,J.A., Schriemer,D.C., Nagel,Z.D. *et al.* (2019) The CHD6 chromatin remodeler is an oxidative DNA damage response factor. *Nat. Commun.*, **10**, 241.
59. El-Khamisy,S.F., Katyal,S., Patel,P., Ju,L., McKinnon,P.J. and Caldecott,K.W. (2009) Synergistic decrease of DNA single-strand break repair rates in mouse neural cells lacking both Tdp1 and aprataxin. *DNA Repair (Amst.)*, **8**, 760–766.
60. Basunia,M.S. (2006) Nuclear Data Sheets for A = 237. *Nucl. Data Sheets*, **107**, 2323–2422.
61. Berger,N.D., Stanley,F.K.T., Moore,S. and Goodarzi,A.A. (2017) ATM-dependent pathways of chromatin remodelling and oxidative DNA damage responses. *Philos. Trans. R. Soc. Lond. B Biol. Sci.*, **372**, 20160283.
62. Lobrich,M., Shibata,A., Beucher,A., Fisher,A., Ensminger,M., Goodarzi,A.A., Barton,O. and Jeggo,P.A. (2010) gammaH2AX foci analysis for monitoring DNA double-strand break repair: strengths, limitations and optimization. *Cell Cycle*, **9**, 662–669.
63. Roukos,V., Pegoraro,G., Voss,T.C. and Misteli,T. (2015) Cell cycle staging of individual cells by fluorescence microscopy. *Nat. Protoc.*, **10**, 334–348.
64. Stiff,T., O'Driscoll,M., Rief,N., Iwabuchi,K., Lobrich,M. and Jeggo,P.A. (2004) ATM and DNA-PK function redundantly to phosphorylate H2AX following exposure to ioninsing radiation. *Cancer Res.*, **64**, 2390–2396.
65. Sykora,P., Witt,K.L., Revanna,P., Smith-Roe,S.L., Dismukes,J., Lloyd,D.G., Engelward,B.P. and Sobol,R.W. (2018) Next generation high throughput DNA damage detection platform for genotoxic compound screening. *Sci. Rep.*, **8**, 2771.
66. Gustafsson,A.S., Hartman,T. and Stenerlow,B. (2015) Formation and repair of clustered damaged DNA sites in high LET irradiated cells. *Int. J. Radiat. Biol.*, **91**, 820–826.
67. Azqueta,A., Langie,S.A.S., Boutet-Robinet,E., Duthie,S., Ladeira,C., Moller,P., Collins,A.R. and Godschalk,R.W.L. (2019) DNA repair as a human biomonitoring tool: Comet assay approaches. *Mutat. Res.*, **781**, 71–87.
68. Wulbrand,C., Seidl,C., Gaertner,F.C., Bruchertseifer,F., Morgenstern,A., Essler,M. and Senekowitsch-Schmidtke,R. (2013) Alpha-particle emitting 213Bi-anti-EGFR immunoconjugates eradicate tumor cells independent of oxygenation. *PLoS One*, **8**, e64730.
69. Oliai,C. and Yang,L.X. (2014) Radioprotectants to reduce the risk of radiation-induced carcinogenesis. *Int. J. Radiat. Biol.*, **90**, 203–213.
70. Charles,C., Nachtergael,A., Ouedraogo,M., Belayew,A. and Duez,P. (2014) Effects of chemopreventive natural products on non-homologous end-joining DNA double-strand break repair. *Mutat. Res. Genet. Toxicol. Environ. Mutagen*, **768**, 33–41.
71. Barnes,S. (1997) The chemopreventive properties of soy isoflavonoids in animal models of breast cancer. *Breast Cancer Res. Treat.*, **46**, 169–179.
72. Dittmann,K., Toulany,M., Classen,J., Heinrich,V., Milas,L. and Rodemann,H.P. (2005) Selective radioprotection of normal tissues by Bowman-birk proteinase inhibitor (BBI) in mice. *Strahlenther. Onkol.*, **181**, 191–196.
73. Rostek,C., Turner,E.L., Robbins,M., Rightnar,S., Xiao,W., Obenaus,A. and Harkness,T.A. (2008) Involvement of homologous recombination repair after proton-induced DNA damage. *Mutagenesis*, **23**, 119–129.